Citation for published version:
Bulathsinghala, D, Wang, Z & Gursul, I 2019, 'Modified near-wakes of axisymmetric cylinders with slanted base', *Aerospace Science and Technology*, vol. 86, pp. 351-363. https://doi.org/10.1016/j.ast.2019.01.022

DOI:
10.1016/j.ast.2019.01.022

Publication date:
2019

Document Version
Peer reviewed version

Link to publication

Publisher Rights
CC BY-NC-ND

University of Bath

General rights
Copyright and moral rights for the publications made accessible in the public portal are retained by the authors and/or other copyright owners and it is a condition of accessing publications that users recognise and abide by the legal requirements associated with these rights.

Take down policy
If you believe that this document breaches copyright please contact us providing details, and we will remove access to the work immediately and investigate your claim.

Download date: 23. Jan. 2020

Modified near-wakes of axisymmetric cylinders with slanted base

D. S. Bulathsinghala, Z. Wang and I. Gursul

Department of Mechanical Engineering, University of Bath, Bath, BA2 7AY, UK

Near-wakes of axisymmetric cylinders with slanted base were investigated in wind tunnel experiments for an upsweep angle of 28°. Effects of splitter-plate, cavity, and flaps on the afterbody vortices and separated flow were studied by means of surface pressure and Particle Image Velocimetry measurements. The splitter plate causes more diffused afterbody vortices due to the turbulence ingestion from the separation region. When the slanted base is replaced with a deep cavity, there is weaker roll-up of vorticity due to the lack of streamwise flow and a solid surface. Varying the splitter plate length in the range tested did not have significant influence on the flowfield, apart from affecting the strength of the splitter-plate vortex. With the splitter plate and cavity, unsteadiness is dominated by the flow separation region, as opposed to the afterbody vortices in the baseline case. A pair of vertical flaps attached to the side-edges of the splitter plate can reduce the unsteadiness at the measurement plane immediately downstream of the splitter plate.

I. Introduction

Complex three-dimensional time-averaged vortex systems have been observed in the near-wake of three-dimensional bluff bodies. For a square-back Ahmed model, both experiments (Evrard et al., 2016) and simulations (Lucas et al., 2017) suggest that the structure of the mean vortex system and its interaction with the bluff body base affect the drag force. A skewed torus shaped mean vortex causes asymmetric pressure on the flat base (Lucas et al., 2017). When there is a base slant, stationary afterbody vortices may form along the inclined edge (Ahmed, 1983; Bearman, 1980) and cause increased drag, depending on the slant angle. Bluff bodies with slanted base and afterbody vortices are relevant to road vehicles (Ahmed, 1983; Bearman, 1980) and some types of transport aircraft (Epstein et al. 1994; Bury et al. 2013).

A generic axisymmetric model studied frequently is the cylinder with a slanted base (Morel, 1979; Maull, 1980; Xia and Bearman, 1983; Bulathsinghala et al., 2017). There is a

sudden decrease of the mean drag at a critical upsweep angle, similar to the "drag crisis" observed for the Ahmed body. Depending on the sweep (slant) angle and the spanwise distance between the afterbody vortices, the wake of axisymmetric cylinders and Ahmed body may exhibit completely attached, separated and reattached (separation bubble), or completely separated flow in the body symmetry plane. Hence, three-dimensional complex interactions of the vortical flows may occur.

Separated flow, afterbody vortices, and the interaction between them not only determine the mean drag, but also the flow field characteristics in the near-wake, including the unsteady aspects. Three-dimensional wakes may be sensitive to the geometric modifications. For example, flight of transport aircraft with the cargo door open and airdropping are relevant to the wake structure (Bury et al., 2013). Open door (effectively a splitter plate) and the base cavity are likely to be important. The use of splitter plates for two-dimensional bluff bodies is well-known. Plates attached at the symmetry plane (Bearman, 1965) as well as plates attached asymmetrically or detached (Ozone, 1999) are some examples. Attached plates to the base and offset from the blunt trailing-edge for a three-dimensional bluff body with square-back were studied by Khalighi et al. (2001). Pairs of attached plates to the trailing-edge, forming a single "base cavity", were studied by Evrard et al. (2016) and Lucas et al. (2017); multi-cavities were studied by Martin-Alcantara et al. (2014). Effect of base cavities on the mean drag was investigated for axisymmetric cylinders (Morel, 1979) with blunt-base. It is clear that wakes of square-back bodies can be modified substantially by splitter plates and base cavities.

For bodies with slanted base, stationary afterbody vortices and separated flow region between the vortex pair can be sensitive to the geometrical modifications. For an Ahmed bluff-body with a rear slant angle of 30°, Beaudoin and Aider (2008) observed that flaps located along the side edges as well as along the separation line on the rear slant can cause drag reduction. In particular, the optimal flap angle appeared to prevent the formation of the afterbody vortices. Interaction between the flow separation from the rear slant and the afterbody vortices that formed along the edges was suggested to be a key aspect. Ben-Hamou et al. (2007) investigated active flow control of the flow over the aft-body of a generic transport aircraft. They found that the vortex pair became tighter when the separation bubble was eliminated. For an Ahmed body with a rear slant angle of 25°, Fourrie et al. (2011) found that an optimally deflected flap along the separation line on the rear slant can not only control the separated region, but also the formation of the afterbody vortices and the total drag. For an axisymmetric cylinder with a slanted base (sweep angle of 28°, Bulathsinghala et al. 2018), the

baseline flow in the symmetry plane appeared to be completely attached. Small flaps (or spoilers) that are placed perpendicularly on the slanted surface induced flow separation and also modified the structure and trajectory of the afterbody vortices. Depending on the streamwise location of the flap, competition between various effects determine the total drag: flap-induced separation, more diffused afterbody vortices due to turbulence ingestion, and displacement of the vortex trajectory away from the surface. It was shown that an optimal streamwise location of the flap exists.

All these previous studies suggest that three-dimensional wakes of bodies with slanted base strongly depend on the characteristics of flow separation along the slanted surface. In this paper, we focus on axisymmetric cylinders with slanted base and investigate the effects of various geometrical modifications. These include splitter plates, flaps and cavities. Keeping in mind that plates and cavities are found for transport aircraft with open door and airdropping, we do not focus on the drag force as these geometrical modifications are necessity and drag reduction is not the goal. Instead, understanding of the flow characteristics and unsteadiness of the near-wake is the main aim. Wind tunnel experiments have been performed to investigate the near-wake of a slanted axisymmetric cylinder with splitter plates, cavities and flaps.

II. Experimental Techniques

The experiments were carried out within the closed return wind tunnel at the Department of Mechanical Engineering, University of Bath. The tunnel has an octagonal cross section with overall dimensions 2.13 m x 1.52 m x 2.70 m with a freestream turbulence intensity below 0.4%. The freestream velocity in the working section was monitored using a pitot tube mounted within the tunnel connected to a digital manometer. The experiments were carried out at $U_\infty = 15$ ms^{-1}.

A. Wind tunnel models

The axisymmetric cylindrical model with slanted base utilized for the experiments had an afterbody upsweep angle $\Phi = 28°$ (see Figure 1(a)). The cylindrical fuselage had a diameter $D = 200$ mm, which resulted in a Reynolds number based on the diameter $Re_D = 200{,}000$. The cylindrical section was fabricated from PVC pipe. The pipe was machined to obtain the required upsweep angle and the base was covered using a 3 mm thick PVC sheet in order to create the elliptical base of the upsweep. To examine the effect of the cavity, an identical second model was manufactured, without the base PVC sheet, which resulted in a full cavity along the

afterbody upsweep. Since the model is hollow, the cavity can be considered to be "deep". A nose-cone was 3D printed using solid laser sintering, which consisted of an ellipsoid of 2:1 major to minor axis ratio. The length between the nose and the upsweep apex was three times the model diameter. The model parameters and coordinate axes can be identified in Figure 1(a).

A streamlined support structure enabled mounting the model within the wind tunnel, and allowed pressure taps to be fed through. In considering various support structures, using a rigid support system to prevent model vibrations was the primary objective, since highly unsteady flow was expected in the afterbody wake. We chose a symmetric support airfoil with a thickness-to-chord ratio of 9% and a maximum thickness of 40 mm (20% of the model diameter), which also facilitated feeding of pressure tubes through the support. The combined blockage effect of the model and the support system was 2% of the working section area. We note that there is always potential risk of support interference on the near-wake. For example, it was shown that the mounting of the body or perturbations introduced into the wake may affect the wake dynamics for a 3D blunt body with an axisymmetric trailing-edge (Grandemange et al. 2012) and for a sphere (Vilaplana et al. 2013). Mariotti et al. 2017 and Mariotti 2018 found junction vortices that formed between the streamlined support and the main axisymmetric bluff bodies with blunt-base and with rear boat tail. However, all these examples had axisymmetric body shapes. In our case of the axisymmetric cylinder with the slanted base, afterbody vortices over the slanted surface are shielded from the wake of the streamlined support (and any potential junction vortices), which are above the top surface of the model (see Figure 2). Hence, we expect minimal effect of the support structure. In our previous study using the same support structure (Bulathsinghala et al 2017), we compared the mean drag coefficient with other experiments reported in the literature which used different supporting mechanisms (wire supports – Xia and Bearman 1983, magnetic supports – Britcher and Alcorn 1991). The results showed good agreement with previous studies, suggesting that the support mechanism used in the present experiment did not have a major influence on the slanted cylinder model drag, at least in the time-averaged sense. In addition, the symmetry checks at a lower Reynolds number in a water tunnel also revealed symmetric time-averaged flowfields (Bulathsinghala et al 2017).

Figure 1(b) presents a schematic of the splitter plate considered. The curved profile of the cross-section of the splitter plate follows the circular contour of the cylindrical model, and the plate is attached at the apex of the upsweep base. Three splitter plates with different lengths were 3D printed using stereolithography process: l/L = 0.30, 0.37 and 0.45. While all three

lengths were used to investigate the effect of splitter plate length on the overall flowfield, for the majority of this investigation the data were obtained for l/L = 0.37. The data also include cases of various flaps attached to the edges of the splitter plate as shown in Figure 1(c). This was investigated to understand the effect on the near-wake. The flap angle was varied as θ = 0°, 33°, 45°, and 90°. The flaps were 3D printed using ABS plastic.

B. Pressure Measurements

Surface pressure measurements were performed on the model without the base cavity and was carried out using a cylindrical 48 port Scanivalve® multiplexer. A Sensortechnics HCX series differential pressure transducer operating within the range -10 mbar to +10 mbar was used to measure the gage pressure. The Scanivalve® was placed above the working section during testing, with the pressure taps fed through the support system. Prior to testing, the transducer was calibrated using a hand held 1 bar rated Druck DPI610 pressure calibrator. Each time-averaged pressure measurement consisted of an average of 3 sets of tap readings, with 1,000 readings per tap in each set. The sampling frequency was 1 kHz and the sampling length was 1 second. A LABVIEW® interface allowed the settling delay between tap measurements to be adjusted, which had to be set accordingly owing to the large length of tubing between the upsweep surface and the transducer above the working section.

C. Particle Image Velocimetry

The 2D PIV system utilized for the experiments was a commercial TSI® system which consists of a TSI® 610036 synchroniser connected to a 200 mJ Nd:YAG laser. A six jet TSI® 9307 oil droplet generator was used to seed the wind tunnel, where the resulting mean seeding particle diameter was about 1 µm. PIV measurements in cross-flow planes were performed on the model at 5 different stations along the afterbody at x/L = 0.2, 0.4, 0.6, 0.8 and 1.0, which can be identified in Fig. 1a. Image capturing was achieved using a 105 mm f/2.8D Nikon lens attached to a 8MP Powerview Plus CCD camera capturing 500 instantaneous image pairs at a capture frequency of 3.75 Hz. The time between image pairs was 8 µs. Due to the low sampling frequency of the PIV measurements, the velocity measurements are not time-accurate. Image processing was achieved using the TSI® Insight 3G software, and the Hart cross-correlation algorithm was applied with a 48x48 interrogation area with 50% overlap. Spatial resolution varied between 0.9 mm and 1.4 mm between measurements, less than 1% of model fuselage

diameter. Assuming flow symmetry, the starboard side vortex was captured in the crossflow PIV results. The PIV camera was positioned downstream of the model within a transparent perspex box with the laser mounted on a traverse system perpendicular to the freestream (see Figure 2(a)).

In addition to the measurements in the cross-flow PIV planes, measurements were made in the model symmetry plane ($z = 0$). The camera was mounted outside the tunnel working section on the starboard side which was equipped with viewing windows. The laser sheet was shined from underneath the tunnel working section (Figure 2(b)). Within this plane, image capturing was achieved using a 50 mm f/1.8D Nikon lens. PIV image processing settings were the same as before, allowing for 4 mm spatial resolution. The estimated uncertainty for velocity measurements was 2% of the freestream velocity.

III. Results and Discussion

A. Splitter plate and base cavity

The effect of adding a splitter plate ($l/L = 0.37$) to the slanted base cylinder model will first be examined. The baseline flowfield refers to the slanted base cylinder afterbody flowfield without the introduction of the splitter plate. Figure 3 presents the pressure measurements for the baseline flowfield and with the $l/L = 0.37$ splitter plate. Figure 3(a) shows the layout of the pressure taps on the slanted surface of the model. The density of taps increases in the local spanwise (z') direction in order to capture the baseline vortex flow footprint. For the pressure measurements of the baseline model (Figure 3(b)), the low pressure region due to the afterbody vortex can be identified towards the outboard edge of the slanted surface. It is seen to exist until around $x/c = 0.40$ while the vortex footprint is visible until around $x/c = 0.60$ beyond which the surface pressure increases as it recovers back to freestream values towards the trailing-edge.

With the introduction of the splitter plate (Figure 3(b)), there is a large region of low pressure present across the span until $x'/c = 0.60$, evident of flow separation due to the plate. There is also an indication of an afterbody vortex forming with a vortex footprint present towards the outboard edge of the slanted surface, present until $x'/c = 0.80$. The features of this vortex footprint appear distinctly different from that of the baseline footprint discussed previously. The pressure distribution in the symmetry plane ($z' = 0$) shown in Figure 3(c)

reveals that the splitter plate causes lower pressure compared to the baseline case. The sudden increase of the surface pressure compared to the baseline case around $x'/c = 0.60$ signals a change in the mean flow topology, which will be discussed with the velocity measurements.

Figure 4 presents the time-averaged streamwise vorticity for the baseline (Figure 4(a)), with the $l/L = 0.37$ splitter plate (Figure 4(b)), and with the base cavity in the presence of the splitter plate (Figure 4(c)). The results are presented as a 3D perspective view. The dotted lines on the upsweep surface represent the locations of the laser sheets at each PIV measurement plane. The baseline flowfield in Figure 4(a) reveals the nature of the baseline afterbody vortex formation. The shear layer roll-up of the vortex appears complete by the third measurement plane, $x/L = 0.6$, and the resulting axisymmetric vortex core region gradually moves away from the surface towards the trailing-edge ($x/L = 1.0$) where the fully developed afterbody vortex is present. Detailed discussion regarding the baseline flowfield can be found in Bulathsinghala et al. (2017). With the introduction of the splitter plate (Figure 4(b)), the afterbody vortex forms further outboard at the first two measurement stations ($x/L = 0.2$ and 0.4). Towards the trailing-edge, the resulting afterbody vortex is diffused in comparison to the baseline case. This is likely to be due the ingestion of turbulence within the separated flow region into the afterbody vortices. A similar effect occurs for the ingestion of jet turbulence into the tip vortices (Margaris et al., 2008; Margaris and Gursul, 2010). The splitter-plate vortex can be seen developing at the first two measurement stations with opposite (positive) vorticity to that of the afterbody vortex. It is noted that the second measurement plane, $x/L = 0.4$ is just downstream of the plate (since $l/L = 0.37$). At the third measurement station, $x/L = 0.6$, the splitter plate vortex appears very diffuse and weak.

Figure 4(c) presents the effect of the base cavity on the flowfield incorporating the splitter plate. With the introduction of the cavity the flow behaviour has changed dramatically. The afterbody vortex in Figure 4(c) is very diffuse and appears weak at the first three measurement planes in comparison to Figure 4(b) (without the cavity but with the splitter plate). However, an axisymmetric region of vorticity characteristic of a fully developed vortex exists at the trailing edge in Figure 4(c), suggesting that there has been a rapid growth in the vortex between $x/L = 0.6$ and $x/L = 1.0$ (trailing-edge). Weak roll-up of vortex at the upstream measurement planes appears to be a result of the cavity flow. Two effects might be contributing to this observation. Firstly, lack of streamwise flow might weaken the vorticity transport through the core. This appears to be an important aspect for the tip/edge vortex control techniques (Gursul and Wang, 2018). Secondly, absence of a solid surface on the model may

strengthen the induced flow near the separation point (edge of the slanted surface), hence effectively decreasing the velocity difference (shear) with the outside.

An interesting feature of the mean flow topology is observed in Figure 4(c) for $x/L \geq 0.6$. There exists a shear layer of opposite (positive) vorticity just outside the primary vortex, which is not observed in Figure 4(b). Figure 5 compares the instantaneous (Fig. 5(a)) and the mean (Fig. 5(b)) velocity vectors in an enlarged view at $x/L = 0.80$ for the cases with and without the cavity. The instantaneous velocity for the cavity case shows the relative location of the shear layer and suggests that it originates from the inside of the cavity. The primary vortex produces a boundary layer on the inner wall of the cylinder, which becomes the source of the opposite-sign vorticity. This flow feature is also present at $x/L = 0.6$ and $x/L = 1.0$, and is a direct consequence of the base cavity.

The variation of the circulation of the time-averaged afterbody vortex is shown in Figure 6 for the baseline, with the splitter plate and the cavity. The circulation calculation considers only the afterbody vortex (negative vorticity), and uses a numerical method executed in MATLAB®. The center of the vortex is first located using the Q-criterion (Hunt et al., 1988; Jeong and Hussain, 1995) as a first step. To calculate the Q-criterion, the deformation tensor, ∇u, is first decomposed into symmetrical and antisymmetrical components; the strain tensor, $S = 0.5(\nabla u + \nabla u^{T})$ and the vorticity tensor, $\Omega = 0.5(\nabla u - \nabla u^{T})$. A vortex is present in the region where $Q = 0.5(\|\Omega\|^2 - \|S\|^2) > 0$. Vortex center is identified as the location of maximum Q value. The circulation within the immediate neighbourhood of this center was then calculated using an area integral of vorticity, before expanding the area outward along the grid by one spatial resolution unit and recalculating the circulation. The calculation was repeated until the change in circulation between iterations was less than 0.5%. Evaluating the circulation using this method overcomes the ambiguity associated with choosing a calculation area in determining the circulation, and the effect of background noise is minimised due to the imposed 0.5% change criterion.

In Figure 6, the baseline vortex circulation increases rapidly until $x/L = 0.6$ while the vortex roll-up is taking place, and then at a slower rate towards the trailing-edge as vorticity is continuously shed into the vortex core. Figure 6 suggests that the splitter plate inhibits the initial growth of the afterbody vortex, showing smaller circulation compared to the baseline case at measurement stations upstream of $x/L = 0.8$. The circulation recovers back to baseline values at $x/L = 0.8$, and at the trailing-edge the resulting vortex has slightly higher circulation

compared to the baseline. With the base cavity, the initial growth in circulation is slower compared to the model without the cavity, until $x/L = 0.6$. There is a rapid increase in circulation between $x/L = 0.6$ and $x/L = 0.8$ when the cavity is present. This is consistent with the time-averaged vorticity presented previously, where the afterbody vortex appeared weak and diffused at the first three measurement planes in particular. Towards the trailing-edge, the circulation continues to increase, with the fully developed vortex at the trailing-edge with the base cavity resulting in a 20% increase in circulation compared to that without the cavity.

Figure 7 shows the time-averaged velocity magnitude with projected streamlines for the same cases. In Figure 7(b), the splitter plate causes two main differences compared to the baseline case in Figure 7(a). The splitter-plate vortex and fast decaying velocity magnitude inboard of the primary vortex are most noteworthy in the first two measurement planes. The introduction of the plate reduces the high crossflow velocity regions seen with the baseline flowfield towards the centreline. With the introduction of the cavity (Figure 7(c)), at $x/L = 0.4$ and 0.6, there is even smaller velocity magnitude between the afterbody vortex and the splitter-plate vortex. The magnitude and regions of high crossflow velocity have been reduced further with the introduction of the cavity. These features of the flow in the near-wake may have important implications for airdropping.

The velocity magnitude, projected streamlines and vorticity of the time-averaged flow in the symmetry ($z = 0$) plane are shown in Figure 8. The baseline flowfield in Figure 8(a) contains no flow separation, with the streamlines following the afterbody shape smoothly. Addition of the $l/L = 0.37$ splitter plate (Figure 8(b)) results in a large region of flow separation, which can be identified by the recirculating streamlines just downstream of the plate. The resulting separation shear layer is identifiable within the time-averaged vorticity. The separated flow reattaches at around $x/L = 0.6$ despite the large region of flow separation, and this is consistent with the surface pressure variation discussed previously in Figure 3. With the base cavity present, Figure 8(c) suggests a larger separation region compared to that without the cavity. The recirculating streamline pattern present in Figure 8(c) is distinctly different to that present in Figure 8(b). With the cavity present, the recirculating flow enters the model cavity, whereas without the cavity, the separated region is confined with the model surface. The location of the flow entering the cavity is around $x/L \approx 0.6$. It is worthy to note that the rapid increase in vortex circulation seen previously in Figure 6 occurs between $x/L = 0.6$ and 0.8. The time-averaged vorticity in Figure 8(c) shows that the separated shear layer when the cavity

is present extends further in the streamwise direction into the wake before dissipating compared to Figure 8(b).

B. Unsteady aspects

Unsteady aspects of the near-wake are also important for various considerations. The root-mean-square (RMS) of the fluctuating velocity is shown in Figure 9. The unsteadiness of the baseline vortex core can be identified at each of the measurement planes in Figure 9(a). Maximum RMS velocity typically occurs at the center of the time-averaged afterbody vortex for the baseline case, which can be attributed to the "meandering" behaviour of the streamwise oriented vortices. Introducing the splitter plate (Figure 9(b)) has increased the overall unsteadiness at each of the measurement planes compared to the baseline case. However, the unsteadiness appears to be dominated by the flow separation region. Even when the complete afterbody vortex roll-up is complete at x/L = 1.0 (trailing-edge), unsteadiness appears to be uniformly spread in the afterbody vortex, which is in contrast with that of the baseline case. Apparently, the source of turbulence is the flow separation induced by the splitter plate. In return, this increased unsteadiness is the reason for the diffusion seen in the time-averaged vorticity towards the trailing-edge in Figure 4(b). The RMS of the fluctuating velocity presented in Figure 9(c) with the base cavity shows qualitatively similar features, although the lower levels of unsteadiness at the first three measurement planes are confined to the shear layers. Nevertheless, completely formed afterbody vortex at x/L = 1.0 still displays uniformly spread turbulence.

The proper orthogonal decomposition can be used to extract the dominant flow features that exist in a flowfield (Berkooz et al., 1993). The technique has been widely used in vortex dominated flows (Graftieaux et al., 2001; Wang and Gursul, 2012) and in particular for the tip/edge vortices (Ma et al., 2017; Bulathsinghala et al., 2017; Chen et al., 2018a; Chen et al., 2018b) to reveal the relative energy and structure of the most dominant modes. The present study employs a MATLAB® code that uses the method of snapshots to extract the POD modes (Chen et al. 2012; Chen et al. 2013). Figure 10 presents the most dominant vorticity POD mode for the cases considered. The baseline slanted base cylinder flowfield (Figure 10(a)) reveals the formation of a vortex dipole towards the trailing-edge, which was discussed by Bulathsinghala et al. (2017). It was shown that, together with a second mode containing another dipole orthogonal to the one in the first mode, the first two modes represent the helical

displacement mode with azhimuthal wavenumber $m = 1$ (Bulathsinghala et al. 2017). In fact, this mode is typical for all tip/edge vortices (Edstrand et al., 2016; Ma et al., 2017; Chen et al., 2018a; Chen et al., 2018b).

It can be observed that the dominant POD modes have been altered dramatically with the addition of the splitter plate (Figure 10(b)) and the cavity (Figure 10(c)). The modes at the trailing-edge appear very diffuse in comparison to the baseline, and a vortex dipole cannot be distinctly identified. With the base cavity, Figure 10(c), the measurement planes $x/L = 0.4$, 0.6 and 0.8 all present shear layer modes. The vortex dipole resulting from the splitter plate vortex is present at $x/L = 0.4$ in Figure 10(c).

C. Effect of splitter plate length

The results presented so far were for the splitter plate length $l/L = 0.37$. The influence of plate length was investigated with two other plate lengths, using the model with the base cavity. Figure 11 presents the time-averaged vorticity for the three different plate lengths. The overall flowfield appears very similar with varying plate length within this range. The main differences occur within the first three measurement planes, where the splitter plate vortex appears more coherent and stronger with increasing plate length. This is visible at $x/L = 0.6$, which is expected since a plate with a longer length sheds more vorticity and results in a stronger splitter plate vortex. The afterbody vortex (region of negative vorticity) flow features are very similar for the three lengths, including for the fully developed vortex at the trailing-edge.

The time-averaged vortex circulation for the three different lengths were found to be similar (not presented), this was expected owing to the almost identical time-averaged vorticity. The time-averaged streamwise ($z = 0$) plane flow is presented in Figure 12, showing overall very similar flowfields. The recirculating flow enters into the cavity at around a similar location for all three lengths, and the streamwise extent of the separation shear layer seen within the time-averaged vorticity in Figure 12 is comparable across all three lengths considered.

D. Effect of flaps

Effect of flaps was investigated on the $l/L = 0.37$ splitter-plate, using the model with the base cavity, in order to examine their efficacy in displacing the splitter-plate vortex. The

splitter-plate vortex itself contributes to the crossflow unsteadiness of the overall flowfield, and manipulation of this vortex could result in a reduction of crossflow unsteadiness. The aim was to displace the splitter-plate vortex away from the plate centreline or away from its surface. The schematic of the flap configurations investigated was shown in Figure 1(c). The triangular flaps, much like half delta wings, were tested with the angle $\theta = 0°$ (horizontal) , 33° (tangential to the model curvature), 45°, and 90° (vertical), when viewed from downstream.

Figure 13 presents the time-averaged vorticity for without and with flaps at various angles. For some cases, the laser sheet for the most upstream measurement plane was blocked by the presence of the flap. The masking seen at the second measurement plane immediately downstream of the splitter plate ($x/L = 0.4$) on the same geometries are due to laser reflections off the thin flap edges (since $l/L = 0.37$) entering the image. Each of the four cases changed the location of the splitter-plate vortex compared to Figure 13(a) (without flaps) at $x/L = 0.4$. The results suggest that the splitter-plate vortex has moved away from the surface with increasing flap angle. For all of the flap cases, at $x/L = 0.6$, a diffused splitter plate vortex can be identified. The main afterbody vortex flow features have not changed substantially for the cases considered.

The first measurement plane immediately downstream of the splitter plate, $x/L = 0.4$, was examined further. Figures 14 – 17 compare the time-averaged vorticity, velocity, projected streamlines, RMS of the fluctuating velocity and the most dominant POD (vorticity) mode at this crossflow measurement plane for all cases. The time-averaged vorticity presented in Figure 14 identifies the relative location of the splitter-plate vortex within the crossflow plane. For small flap angles, the splitter-plate vortex is outboard, but close to the surface. With increasing flap angle, the vortex moves inboard and further away from the splitter plate. For $\theta = 90°$, not only is the vortex furthest from the splitter-plate surface, but also appears smaller and weaker. Figure 15 shows the crossflow velocity magnitude with the projected streamlines for the same configurations. For all flap angles, the maximum velocity magnitude is reduced compared to the reference case. The afterbody vortex and the splitter-plate vortex form a dipole, which can be distinctly identified from the streamlines in each case. Note that the region of higher crossflow velocity is mostly confined outside of the flap for $\theta = 90°$. In order to examine the flow unsteadiness, Figure 16 presents the corresponding RMS velocity for all cases. A reduction of overall flow unsteadiness was observed for the $\theta = 90°$ (vertical) flap. Since the splitter-plate vortex is now forming away from the surface, there exists a region of low unsteadiness closer to the surface of the splitter-plate. Figure 17 presents the most dominant

(first) POD mode for all cases. It is seen that all cases apart from Fig. 17b ($\theta = 0°$) exhibit a vortex dipole corresponding to the splitter-plate vortex. The percentage of total energy was obtained from the POD analysis for each case. It was found that the relative energy of the first POD mode decreased as θ is increased, from 13.3% for $\theta = 0°$ to 9.5% for $\theta = 90°$.

IV. Conclusions

Near-wakes of axisymmetric cylinders with slanted base were investigated in the wind tunnel experiments for an upsweep angle of $\Phi = 28°$. Effects of geometrical modifications in the form of splitter plate, cavity and flaps on the afterbody vortices and separated flow in the near-wake were studied by means of surface pressure and velocity measurements. Significant flowfield differences were observed with the introduction of a splitter plate compared to the baseline. The resulting time-averaged vortex was of nearly equal strength but more diffused at the trailing-edge due to the ingestion of turbulence from the flow separation region induced by the splitter plate.

Incorporating a base cavity with the splitter plate results in a more coherent splitter-plate vortex, but also causes a delay in the circulation growth of the afterbody vortex which does not show significant growth until $x/L = 0.8$. The cavity flow causes weaker roll-up of vorticity, due to the lack of streamwise flow and a solid surface. Also, it appears that the primary vortex induces opposite sign of vorticity that sheds from the inner wall of the body. The magnitude of the crossflow velocity is smaller inboard of the vortices with the splitter plate and the cavity. The separated flow region in the symmetry plane is larger with the base cavity present, as the recirculating flow is able to enter the cavity. Varying the splitter plate length between $l/L = 0.30$ and $l/L = 0.45$ did not result in major flowfield changes, apart from generating a more coherent time-averaged splitter plate vortex.

While the baseline case exhibits meandering as the afterbody vortex develops, the splitter plate and cavity cases are dominated by the unsteadiness in the separated flow region. In these cases, it appears that the turbulence in the separated flow is ingested into the afterbody vortex. Various flaps attached to the edge of the splitter plate were examined to understand the effect on the flow and unsteadiness. The vertical flap ($\theta = 90°$) showed the most potential in terms of reduced unsteadiness at the measurement plane immediately downstream of the plate.

For the current study, we have focused on a single upsweep angle of 28 degrees which is comparable to most cargo aircraft with upswept afterbodies. Based on our previous study (Bulathsinghala et al 2017), varying the upsweep angle between 24 degrees and 32 degrees results in about 50% increase in the strength of the vortices. Since the effects of splitter-plate, cavity, and flaps on the afterbody vortices is significant, these modifications may be more pronounced with increasing upsweep angle and vortex strength.

Acknowledgement

This work was supported by the Air Force Office of Scientific Research, Air Force Material Command, USAF, under grant number FA9550-14-1-0126, monitored by Douglas Smith.

References

Ahmed, S. R., 1983, "Influence of base slant on the wake structure and drag of road vehicles", *Journal of Fluids Engineering,* vol. 105, pp. 429-434.

Bearman, P.W., 1965, "Investigation of the flow behind a two-dimensional model with a blunt trailing edge and fitted with splitter plates", *Journal of Fluid Mechanics,* vol. 21, pp. 241-255.

Bearman, P. W., 1980, "Bluff body flows applicable to vehicle aerodynamics," *Journal of Fluids Engineering,* Vol. 102, No. 3, pp. 265-274.

Beaudoin, J.F. and Aider, J.L., 2008, "Drag and lift reduction of a 3D bluff body using flaps", *Experiments in Fluids,* vol. 44, pp. 491–501.

Ben-Hamou, E., Arad, E. and Seifert, A., 2007, "Generic transport aft-body drag reduction using active flow control", *Flow Turbulence Combustion,* vol. 78, pp. 365-382.

Berkooz, G., Holmes, P., and Lumley, J. L., 1993, "The proper orthogonal decomposition in the analysis of turbulent flows", *Annual Review of Fluid Mechanics*, Vol 25, pp. 539-575.

Britcher CP, Alcorn CW (1991) Interference-free measurements of the subsonic aerodynamics of slanted -base ogive cylinders. AIAA J 29:520–525. doi:10.2514/3.10614

Bulathsinghala, D. S., Jackson, R., Wang, Z., and Gursul, I., 2017, "Afterbody vortices of axisymmetric cylinders with a slanted base", *Experiments in Fluids*, 58:60.

Bulathsinghala, D. S., Wang, Z., and Gursul, I., 2018, "Drag reduction by manipulation of afterbody vortices", *Journal of Aircraft,* https://doi.org/10.2514/1.C034957.

Bury, Y., Jardin, T. and Klockner, A., 2013, "Experimental investigation of the vortical activity in the close wake of a simplified military transport aircraft," *Experiments in Fluids*, Vol. 54, No. 5, pp. 1-15.

Chen, H., Reuss, D. L., and Sick, V., 2012, "On the use and interpretation of proper orthogonal decomposition of in-cylinder engine flows", *Measurement Science and Technology*, Vol. 23, No. 8, Article number 085302.

Chen, H., Hung, D. L. S., Reuss, D. L., and Sick, V., 2013, "A practical guide for using proper orthogonal decomposition in engine research", *International Journal of Engine Research*, Vol. 14, No. 4, pp. 307-319.

Chen, C., Wang, Z. and Gursul, I., 2018a, "Experiments on tip vortices interacting with downstream wings", *Experiments in Fluids*, 59:82. https://doi.org/10.1007/s00348-018-2539-7.

Chen, C., Wang, Z. and Gursul, I., 2018b, "Vortex coupling in trailing vortex-wing interactions", *Physical Review Fluids*, vol. 3, 034704 , DOI:10.1103/PhysRevFluids.3.034704

Edstrand, A. M., Davis, T. B., Schmid, P. J., Taira, K., and Cattafesta, L. N., 2016, "On the mechanism of trailing vortex wandering", *Journal of Fluid Mechanics*, Vol 801, pp. 1-11.

Epstein, R. J., Carbonaro, M. C., and Caudron, F., 1994, "Experimental Investigation of the Flowfield About an Upswept Afterbody," *Journal of Aircraft*, Vol. 31, No. 6, pp. 1281–1290. doi:10.2514/3.46648

Evrard, A., Cadot, O., Herbert, V., Ricot, D., Vigneron, R., and Delery, J., 2016, "Fluid force and symmetry breaking modes of a 3D bluff body with a base cavity", *Journal of Fluids and Structures*, Vol. 61, pp. 99-114.

Fourrie, G., Keirsbulck, L., Labraga, L. and Gillieron, P., 2011, "Bluff-body drag reduction using a deflector", *Experiments in Fluids,* vol. 50, pp. 385–395, DOI 10.1007/s00348-010-0937-6

Graftieaux, L., Michard, M., and Nathalie, G., 2001, "Combining PIV, POD and vortex identification algorithms for the study of unsteady turbulent swirling flows", *Measurement Science and Technology*, Vol. 12, No. 9, pp. 1422-1429.

Grandemange, M., Gohlke, M., Parezanovic, V., and Cadot, O. (2012). On experimental sensitivity analysis of the turbulent wake from an axisymmetric blunt trailing edge. Physics of fluids, 24(3):035106.

Gursul, I. and Wang, Z., 2018, "Flow control of tip/edge vortices", *AIAA Journal*, *Special Issue on Flow Control,* http://arc.aiaa.org/doi/abs/10.2514/1.J056586

Hunt, J. C. R., Wray, A. A., and Moin, P., 1988, "Eddies, stream and convergence zones in turbulent flows", *Center for Turbulence Research Report CTR-S88*, Vol. 193.

Jeong, J., and Hussain, F., 1995, "On the identification of a vortex", *Journal of Fluid Mechanics*, Vol. 285, pp. 69-94.

Khalighi, B., Zhang, S., Koromilas, C. Balkanyi, S.R., Bernal, L.P., Iaccarino, G., and Moin, P., 2001, "Experimental and computational study of unsteady wake flow behind a bluff body with a drag reduction device", SAE paper 2001-01B-207.

Lucas, J.–M., Cadot, O., Herbert, V., Parpais, S., and Delery, J., 2017, "A numerical investigation of the symmetric wake mode of a squareback Ahmed body – effect of a base cavity", *Journal of Fluid Mechanics*, Vol. 831, pp. 675-697.

Ma, B.F., Wang, Z. and Gursul, I., 2017, "Symmetry breaking and instabilities of conical vortex pairs over slender delta wings", *Journal of Fluid Mechanics*, vol. 832, pp. 41-72. doi:10.1017/jfm.2017.648

Margaris, P., Marles, D., and Gursul, I., 2008, "Experiments on jet/vortex interaction", *Experiments in Fluids*, vol. 44, no. 2, pp. 261-278.

Margaris, P. and Gursul. I., 2010, "Vortex topology of wing tip blowing", *Aerospace Science and Technology*, vol. 14, issue: 3, pp. 143-160.

Mariotti, A., Buresti, G., Gaggini, G., Salvetti, M.V., 2017, Separation control and drag reduction for boat-tailed axisymmetric bodies through contoured transverse grooves, J. Fluid Mech. 832, 514–549.

Mariotti, A. 2018, Axisymmetric bodies with fixed and free separation: Base pressure and near-wake fluctuations, J. Wind Eng. Ind. Aerodyn. 176, 21–31.

Martin-Alcantara, A., Sanmiguel-Rojas, E., Gutierrez-Montes, C., and Martinez-Bazan, C., 2014, "Drag reduction induced by the addition of a multi-cavity at the base of a bluff body", *Journal of Fluids and Structures*, Vol. 48, pp. 347-361.

Maull, O.J., 1980, "The drag of slanted-based bodies of revolution", *Aeronautical Journal,* vol. 84, no. 833, pp. 164-166.

Morel, T., 1979, "Effect of base cavities on the aerodynamic drag of an axisymmetric cylinder", *Aeronautical Quarterly*, Vol. 30 (Pt. 2), pp. 400-412.

Ozono, S., 1999, "Flow control of vortex shedding by a short splitter plate asymmetrically arranged downstream of a cylinder", *Physics of Fluids*, Vol. 11, No. 10, pp. 2928-2934.

Vilaplana, G., Grandemange, M., Gohlke, M., Cadot, O., 2013. Global mode of a sphere turbulent wake controlled by a small sphere. J. Fluid Struct. 41, 119–126.

Wang, Z., and Gursul, I., 2012, "Unsteady characteristics of inlet vortices", *Experiments in Fluids*, Vol. 53, No. 4, pp. 1015-1032.

Xia, X.J. and Bearman, P.W., 1983, "Experimental investigation of the wake of an axisymmetric body with a slanted base", *Aeronautical Quarterly,* vol. 34, no. 1, pp. 24-45.

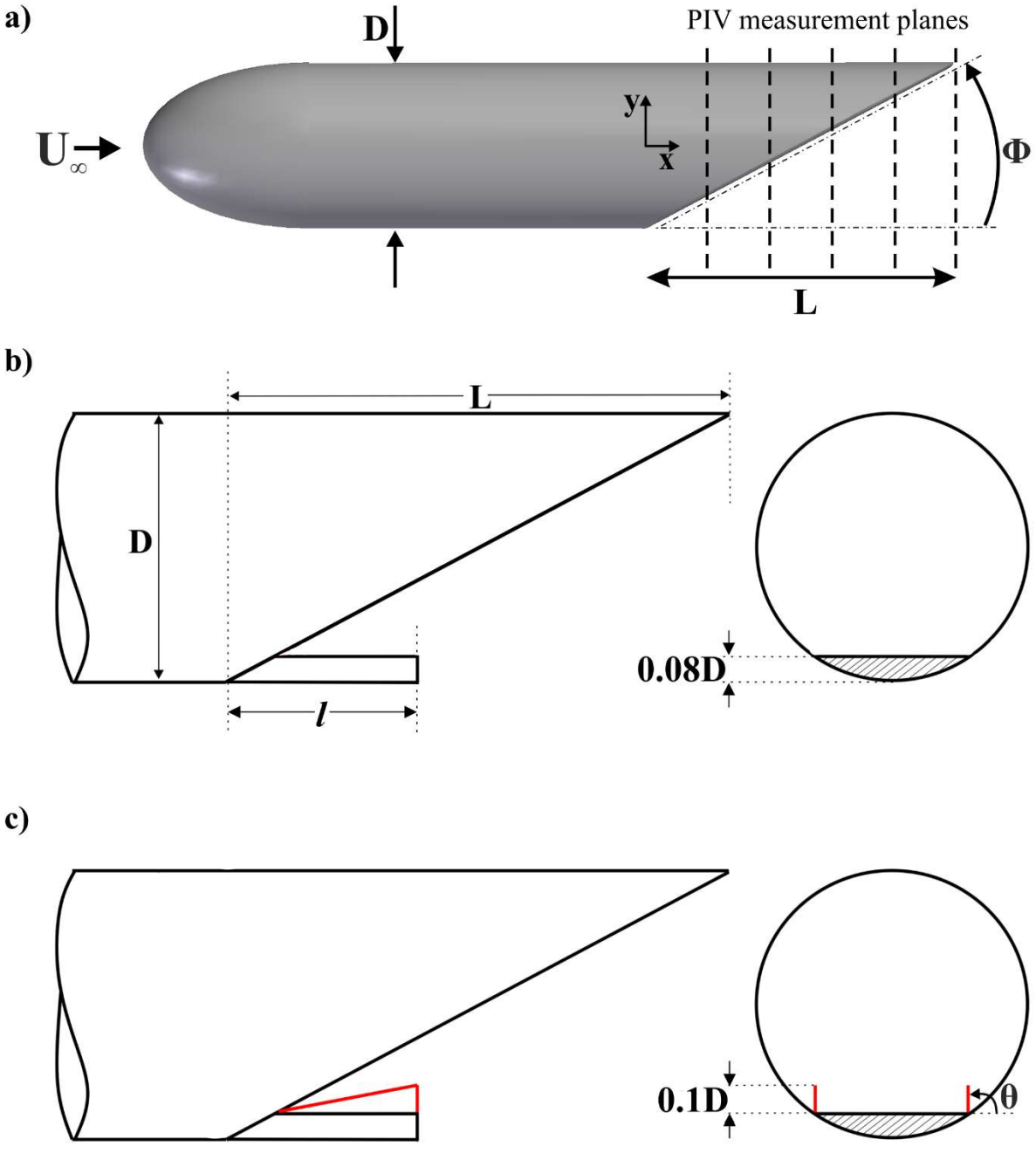

Figure 1: a) Baseline slanted cylinder model and associated coordinate axes, b) schematic of splitter plate, c) schematic of flaps.

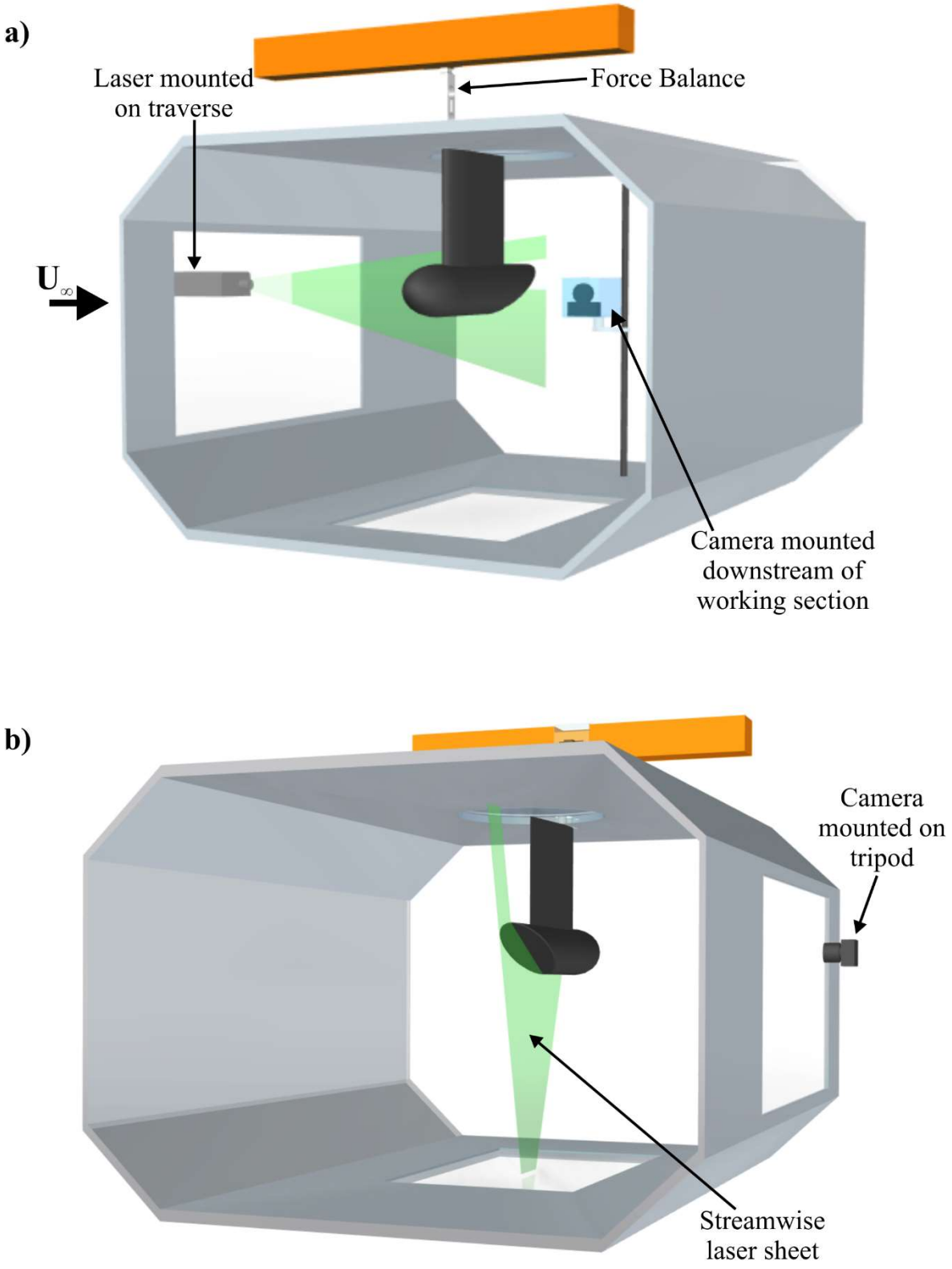

Figure 2: Schematic of PIV setup for measurements in a) cross-flow planes, and b) symmetry plane.

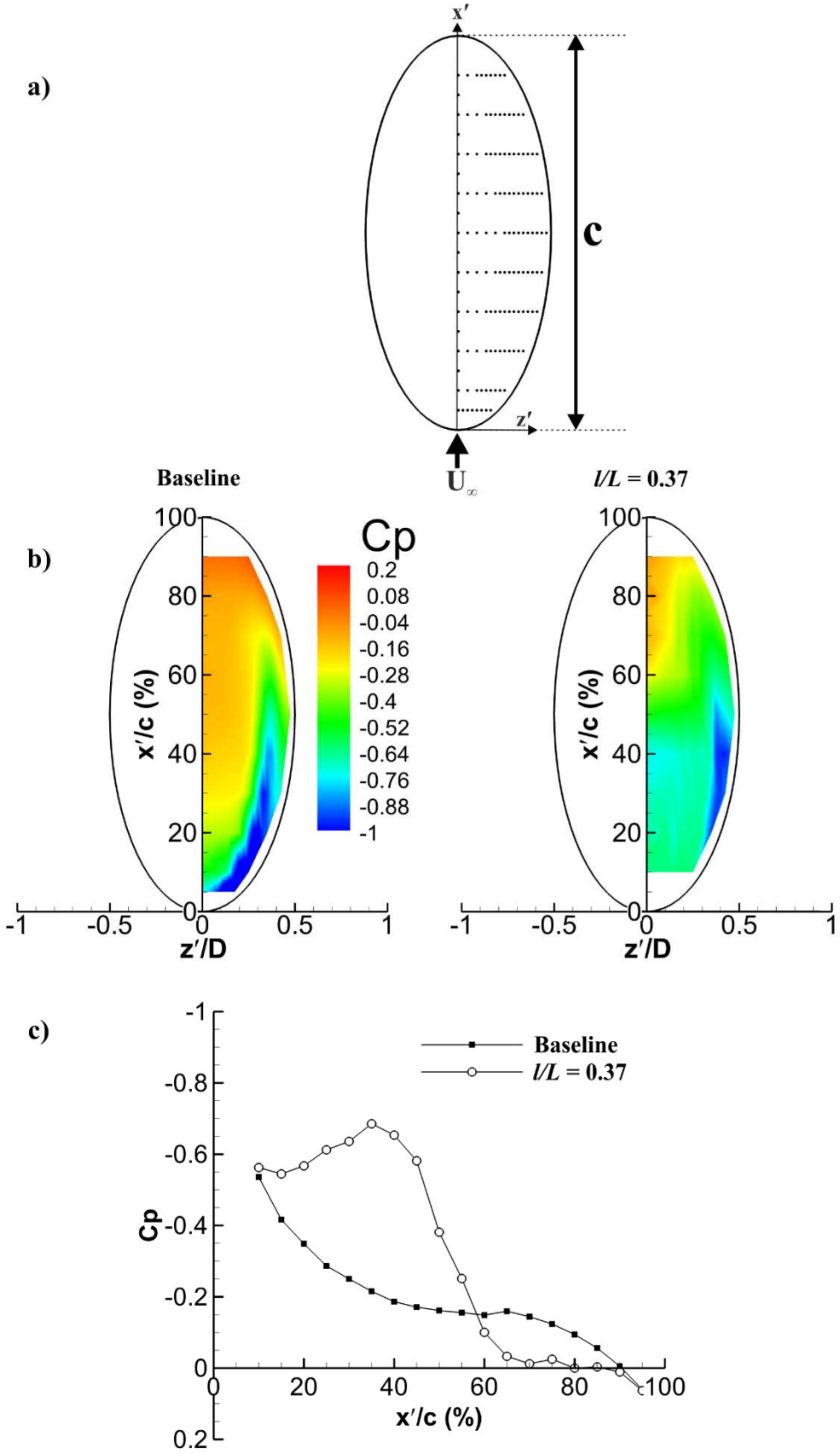

Figure 3: a) Locations of pressure taps, b) surface pressure distributions, and c) variation of surface pressure in the symmetry plane.

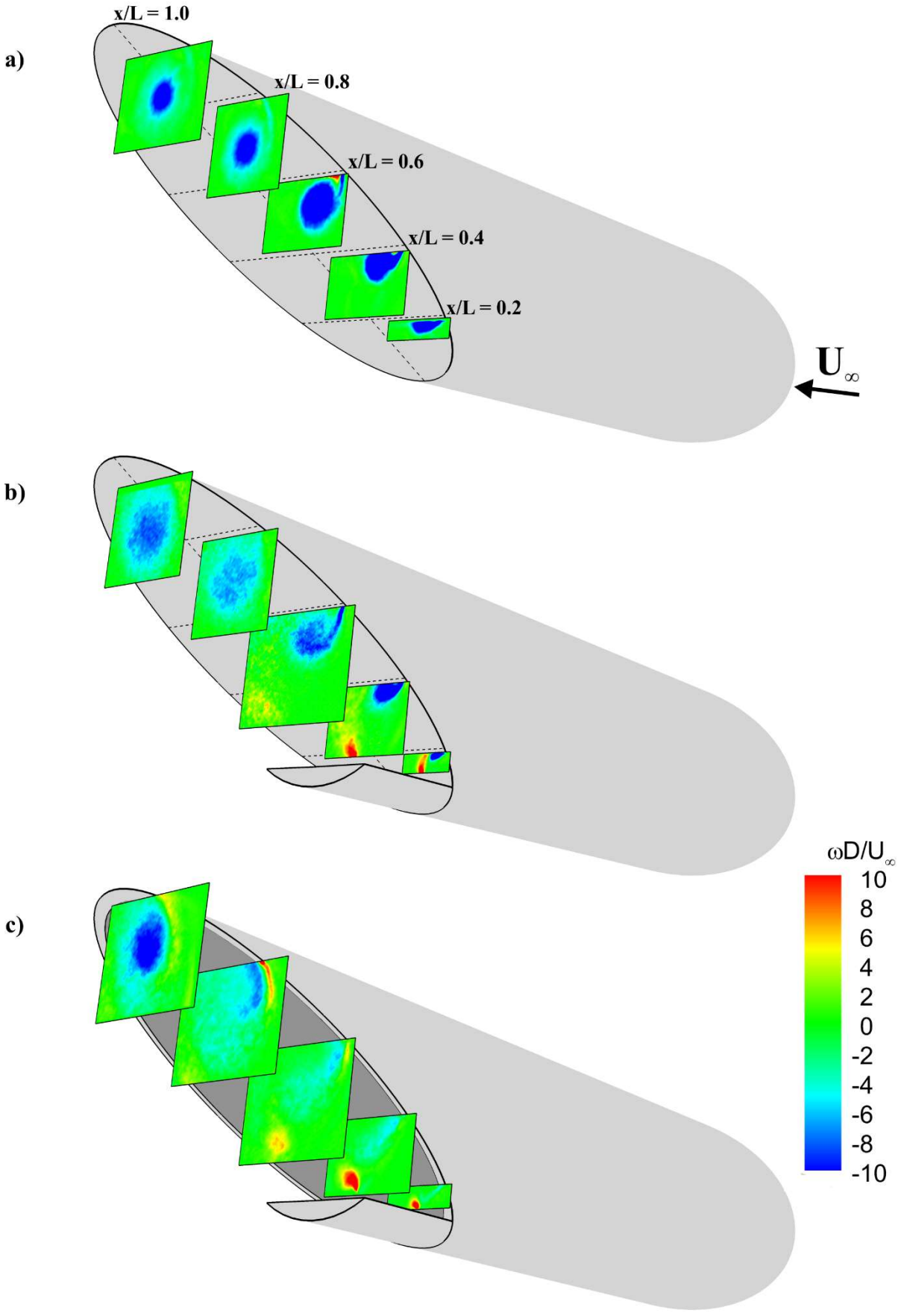

Figure 4: Time-averaged vorticity for a) baseline, b) with splitter plate, and c) with cavity.

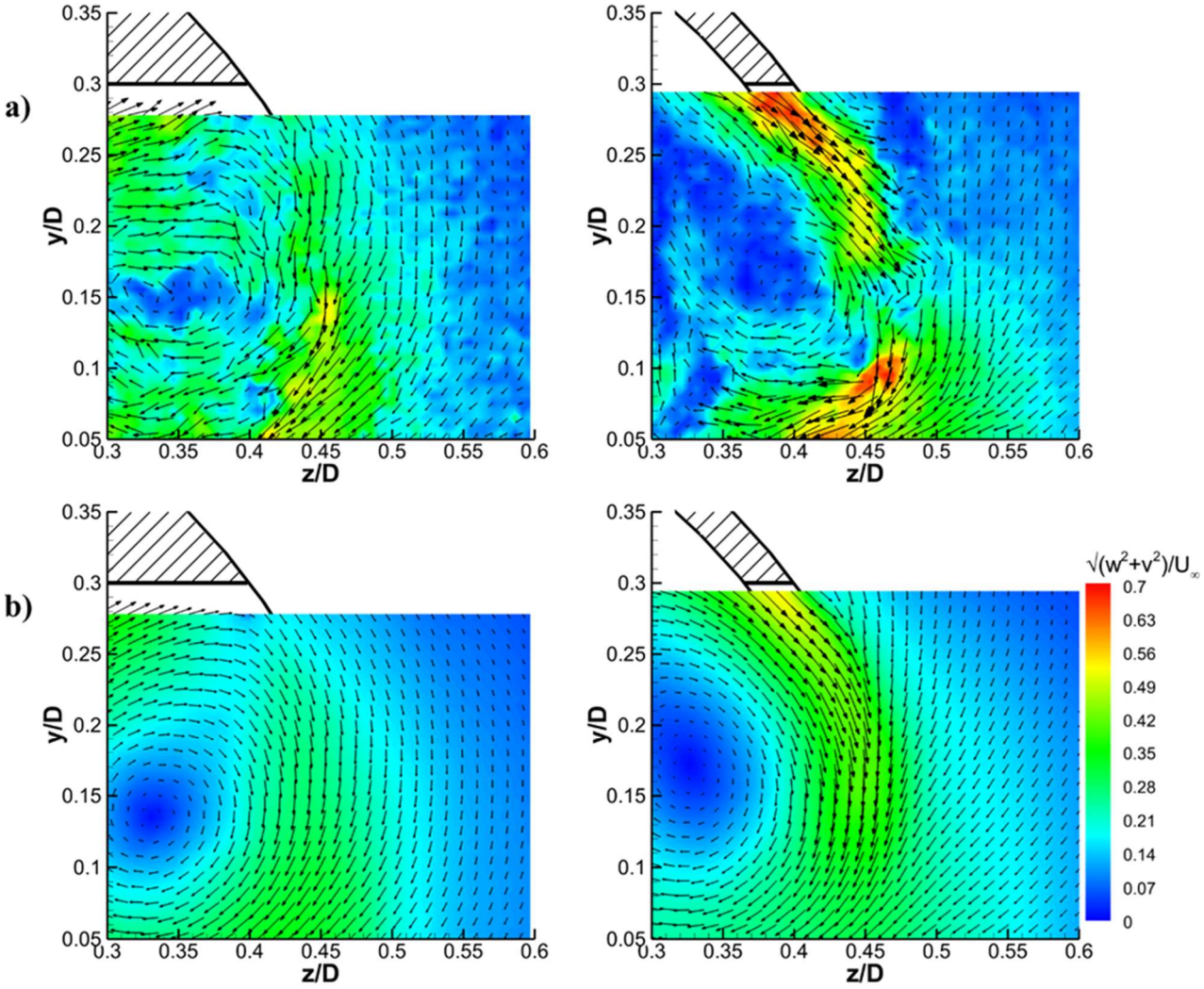

Figure 5: Comparison of velocity vectors and magnitude at $x/L = 0.8$ for without base cavity (left), and with base cavity (right), a) instantaneous flow, and b) time-averaged flow.

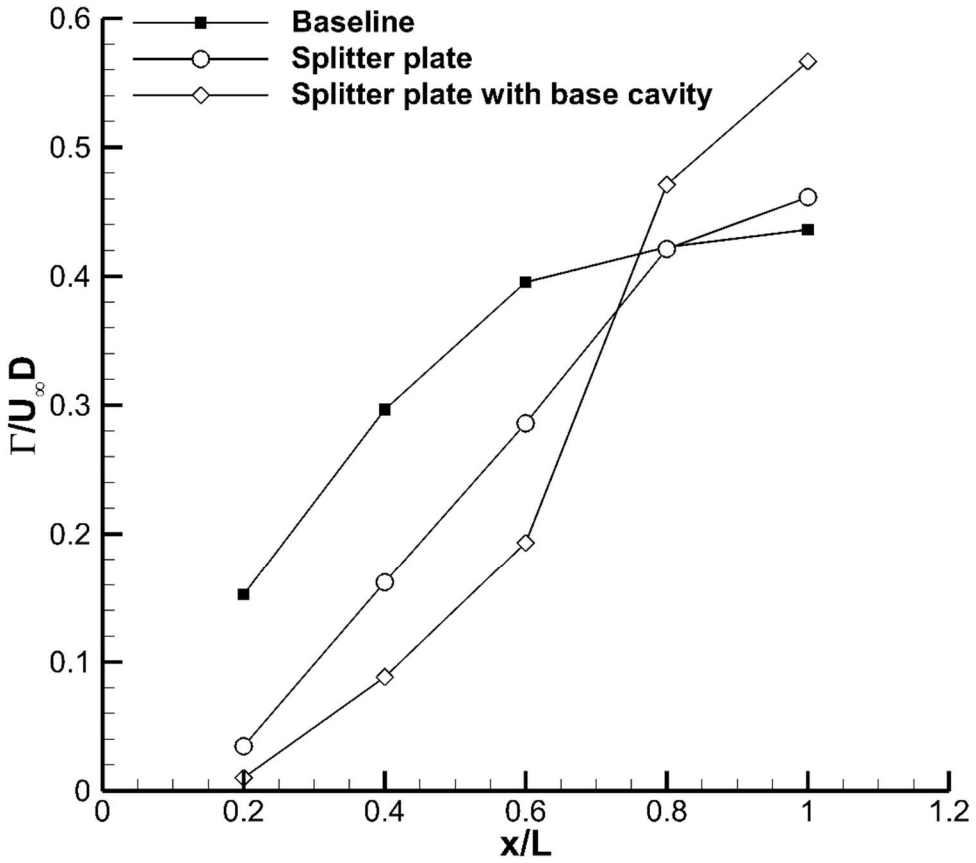

Figure 6: Variation of circulation for baseline, splitter plate and cavity cases.

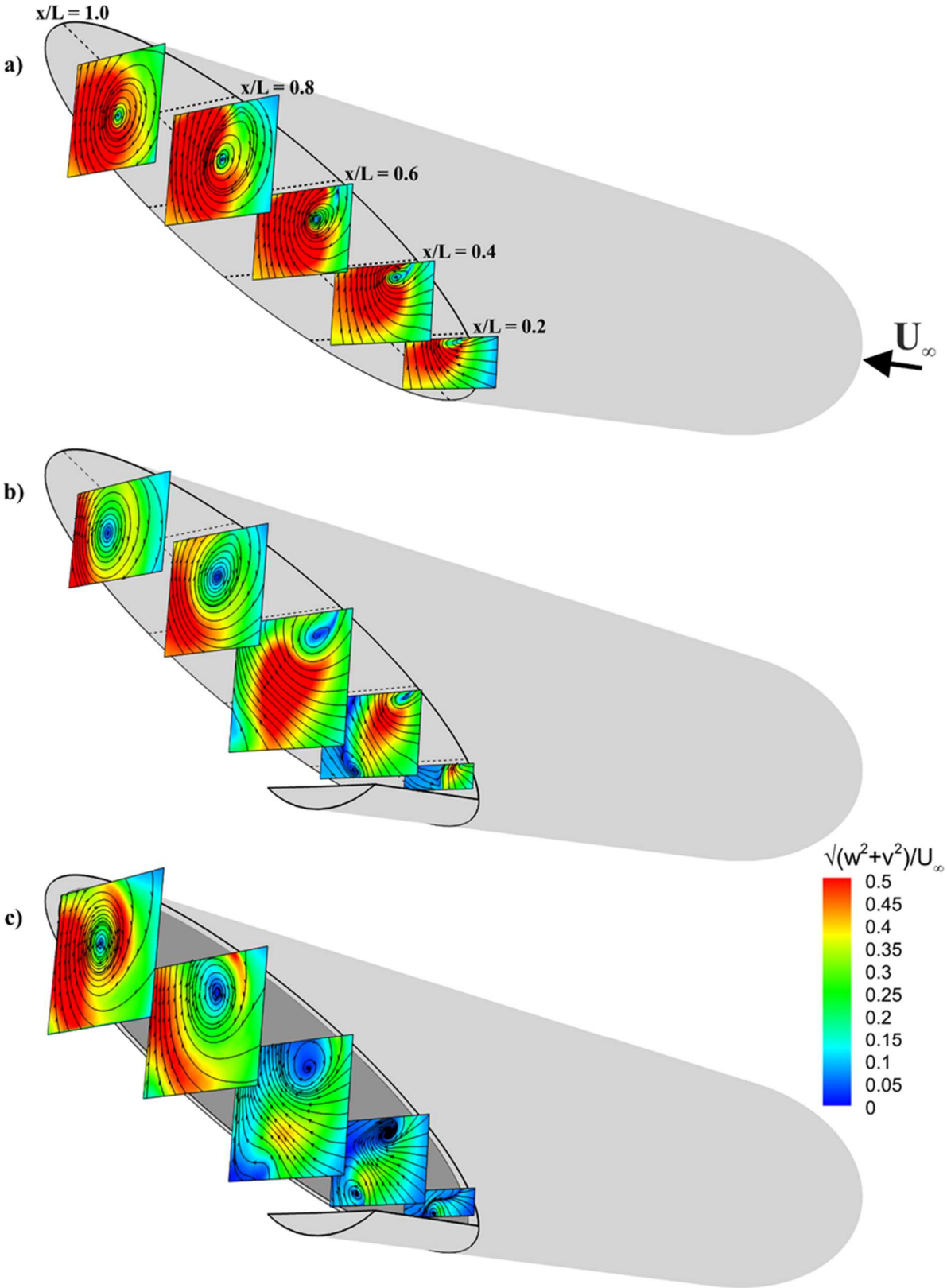

Figure 7: Time-averaged velocity with projected streamlines for a) baseline, b) splitter plate and c) base cavity.

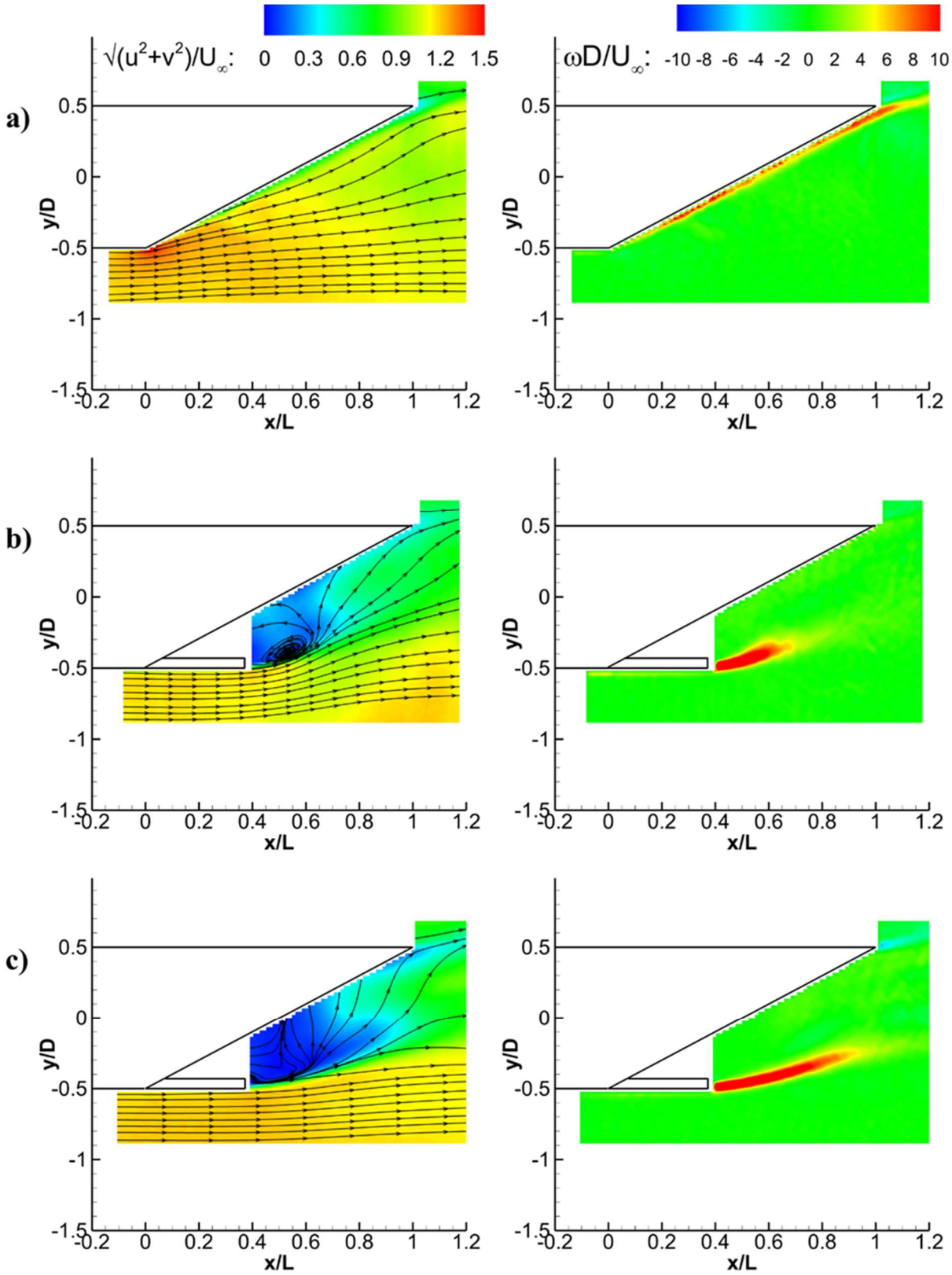

Figure 8: Time-averaged velocity with projected streamlines (left) and vorticity (right) in the symmetry plane for a) baseline, b) splitter plate, and c) base cavity.

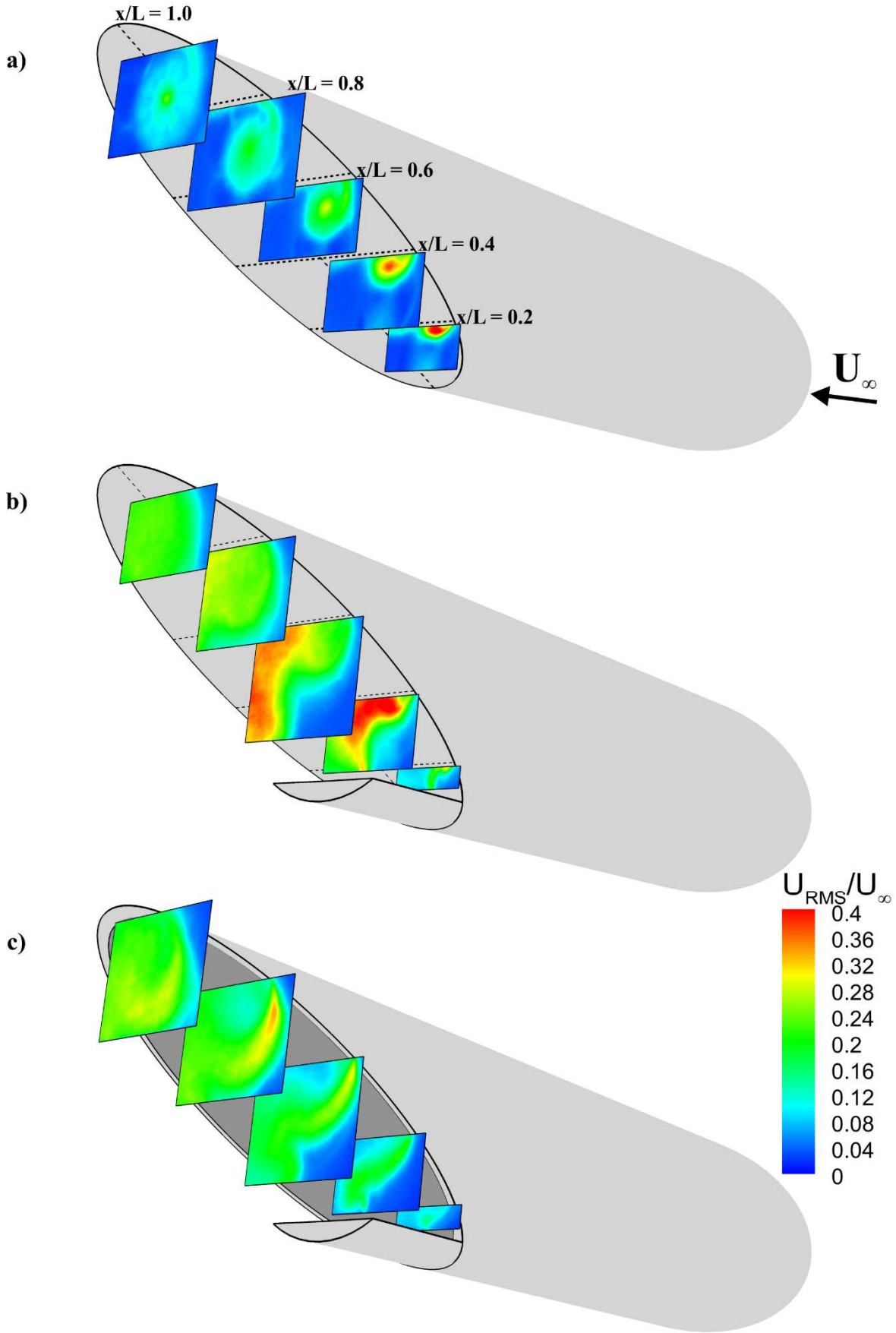

Figure 9: Root-mean-square (RMS) of fluctuating velocity for a) baseline, b) splitter plate, and c) cavity.

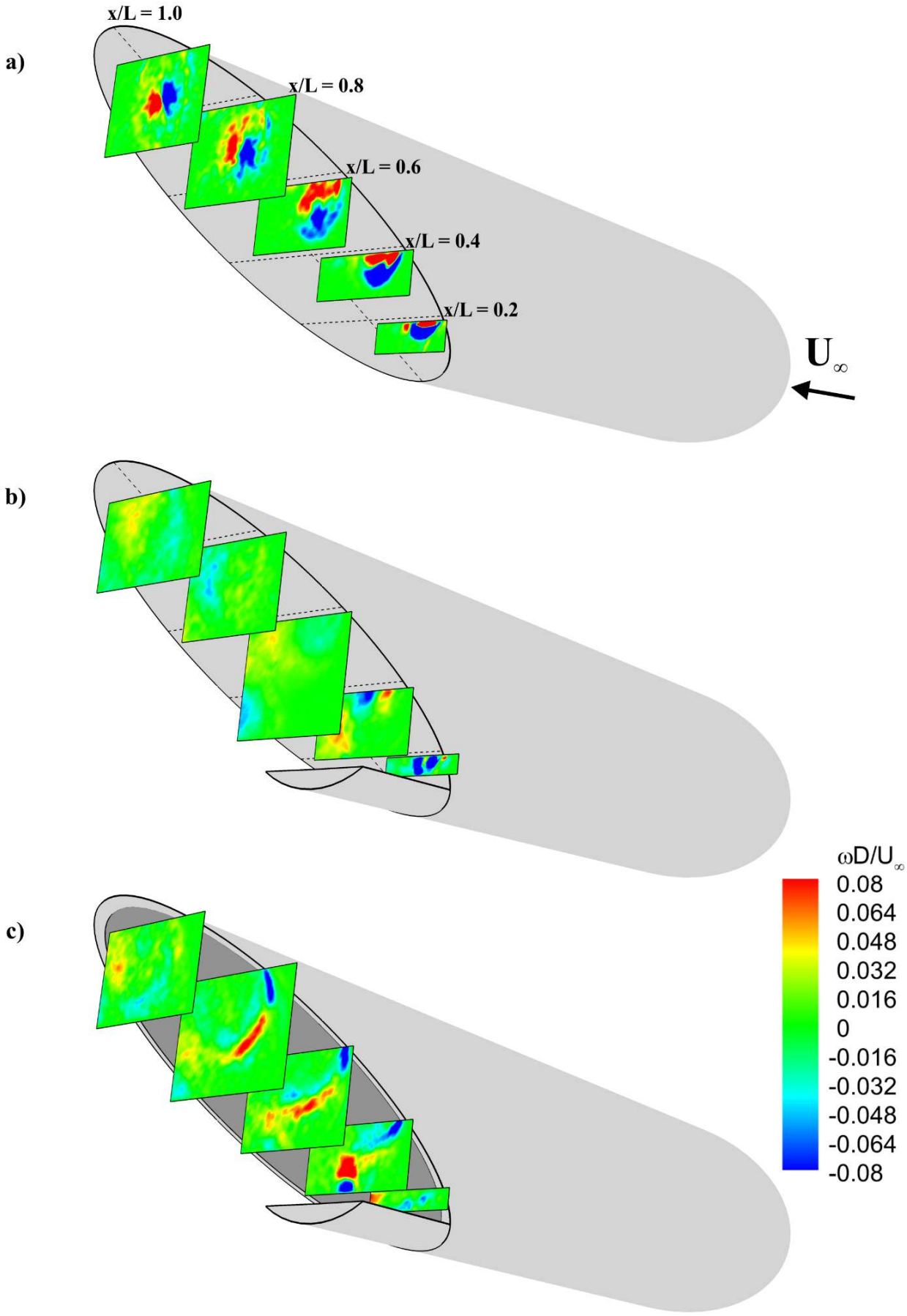

Figure 10: First POD mode for a) baseline, b) splitter plate, and c) base cavity.

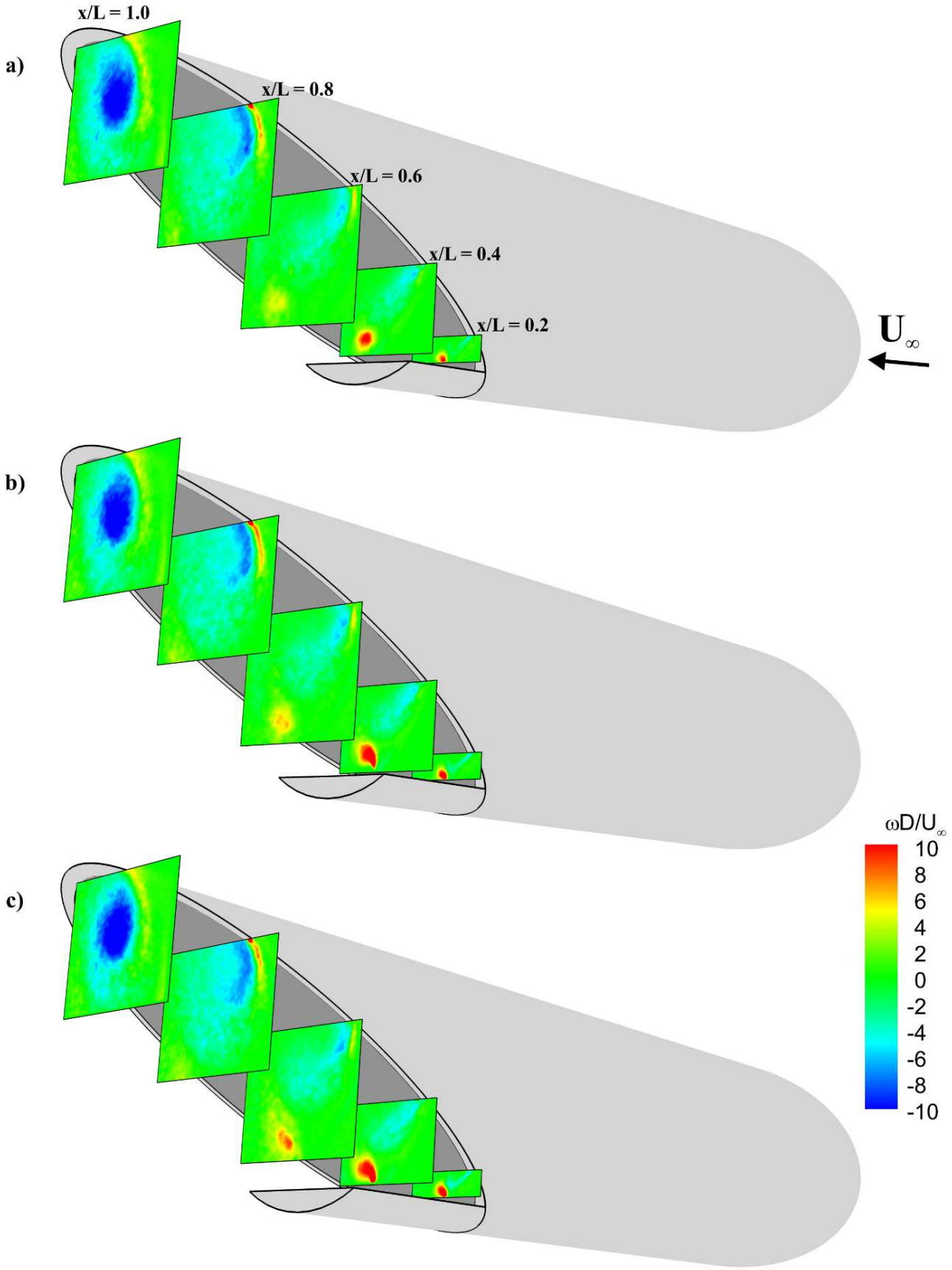

Figure 11: Time-averaged vorticity for a) l/L = 0.30, b) l/L = 0.37 and c) l/L = 0.45.

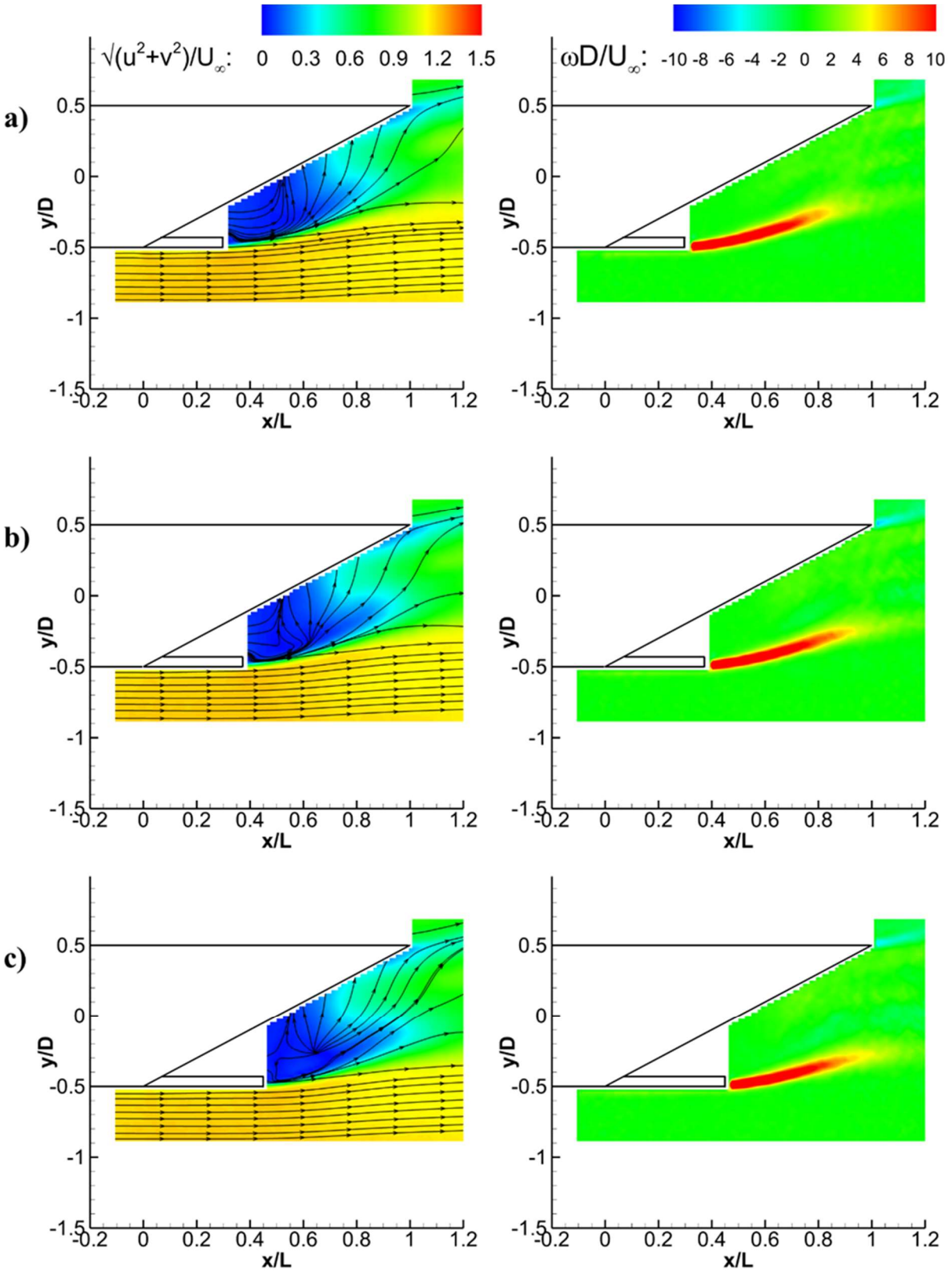

Figure 12: Time-averaged velocity magnitude with projected streamlines (left) and vorticity (right) in the symmetry plane for a) l/L = 0.30, b) l/L = 0.37 and c) l/L = 0.45.

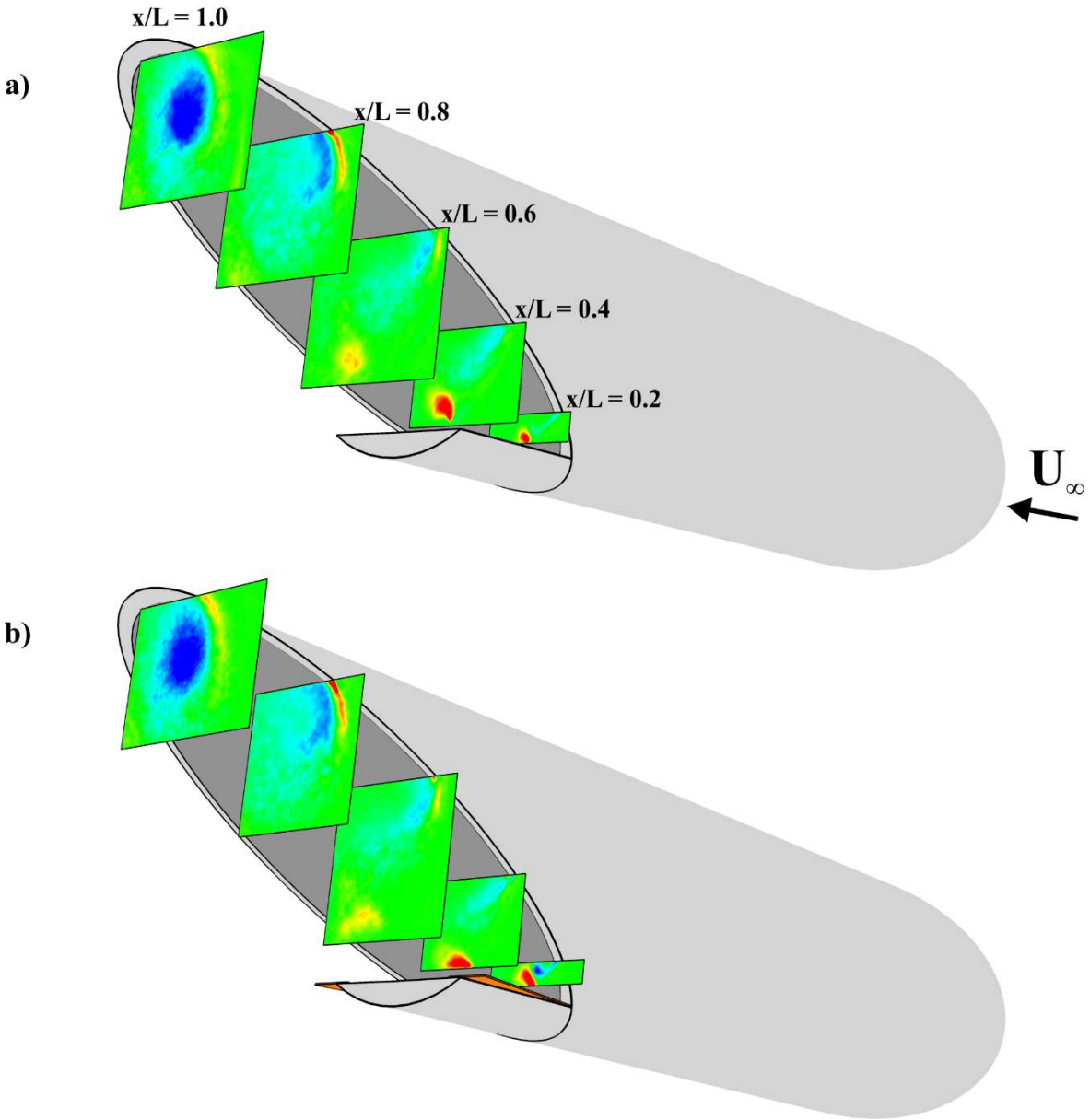

Figure 13: Time-averaged vorticity for a) l/L = 0.37 without flaps, b) θ = 0° horizontal flap, c) θ = 33° tangential flap, d) θ = 45° flap and e) θ = 90° vertical flap.

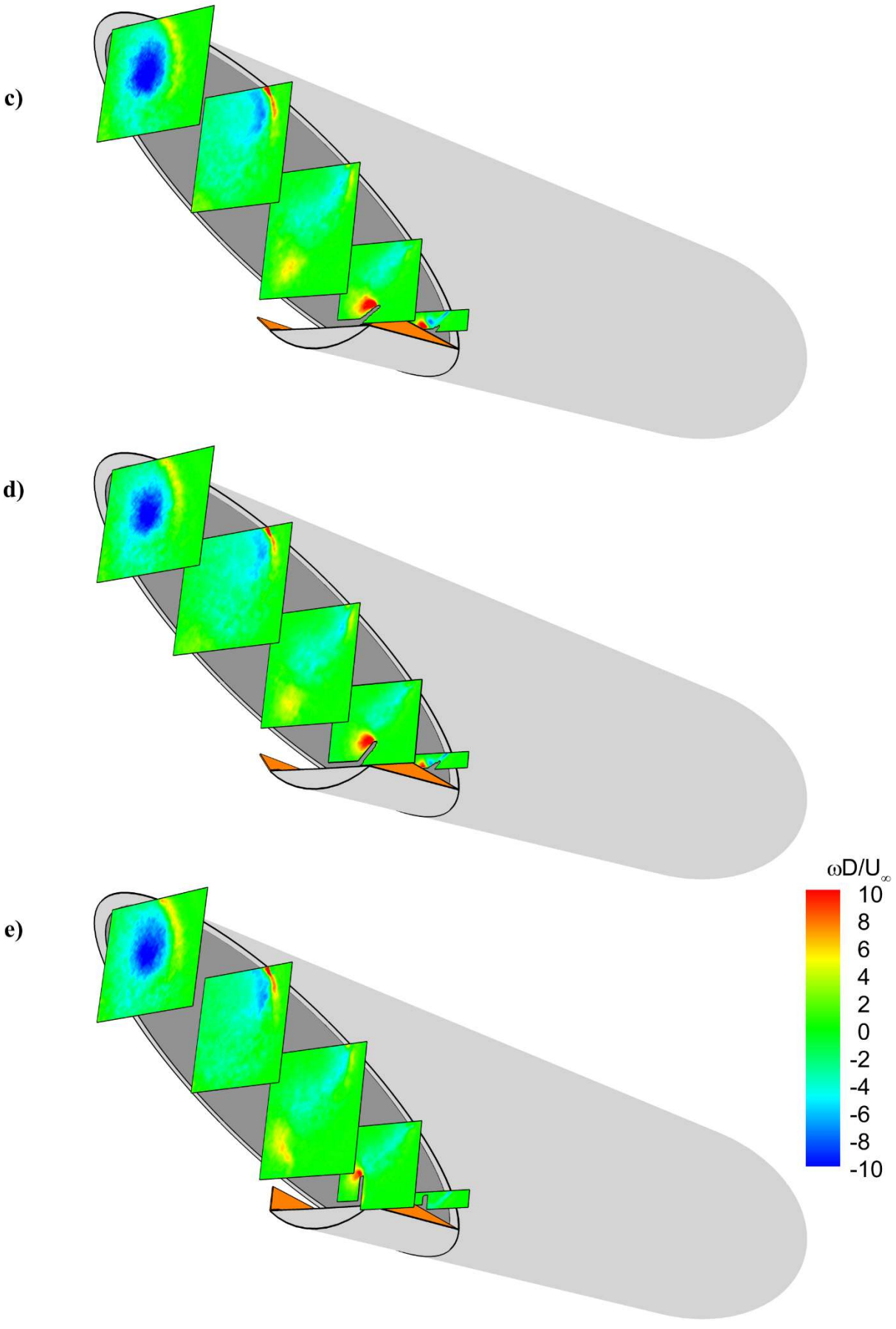

Figure 13: continued.

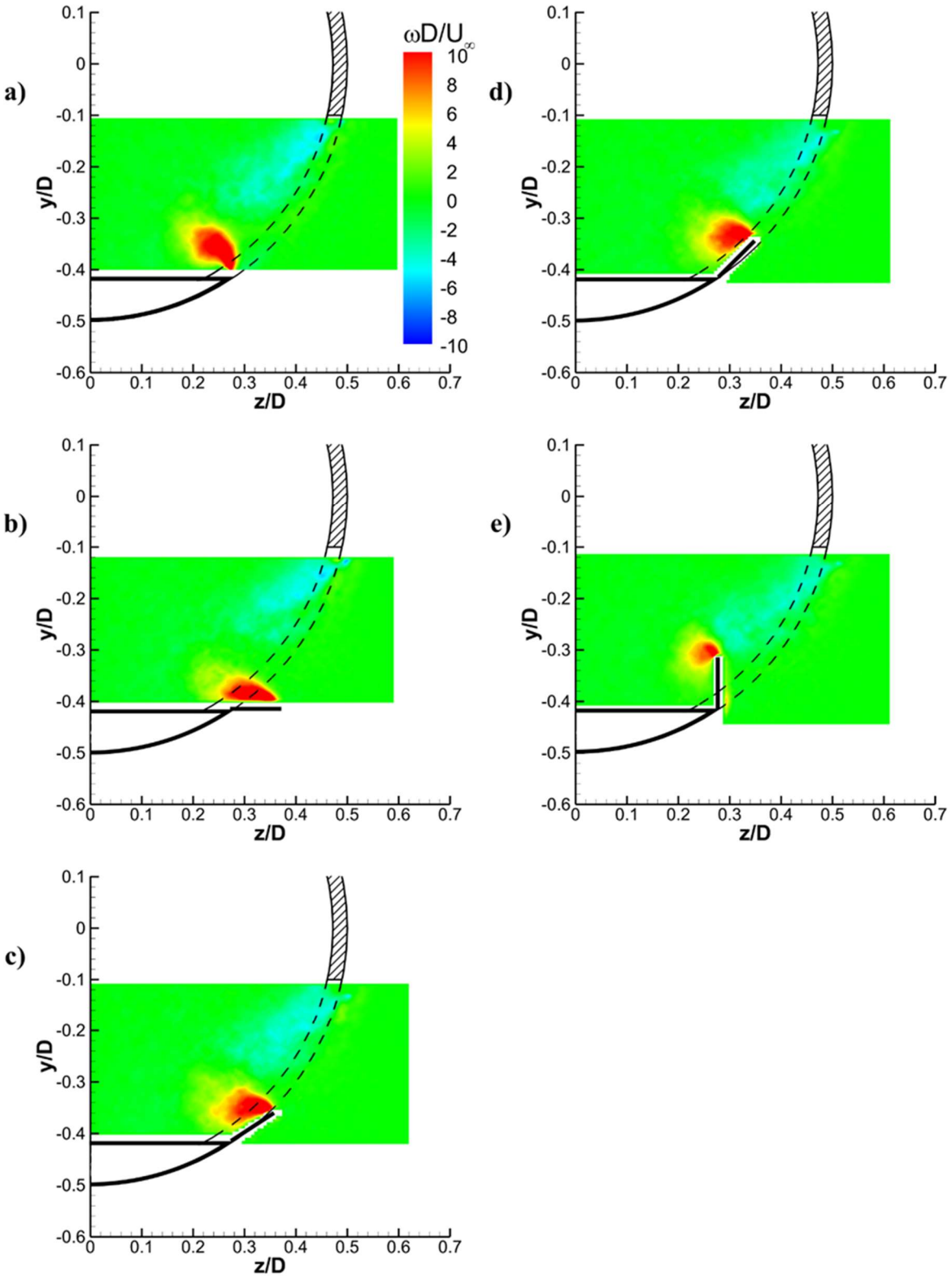

Figure 14: Time-averaged vorticity at $x/L = 0.4$ for a) $l/L = 0.37$ without flaps, b) $\theta = 0°$, c) $\theta = 33°$, d) $\theta = 45°$, and e) $\theta = 90°$.

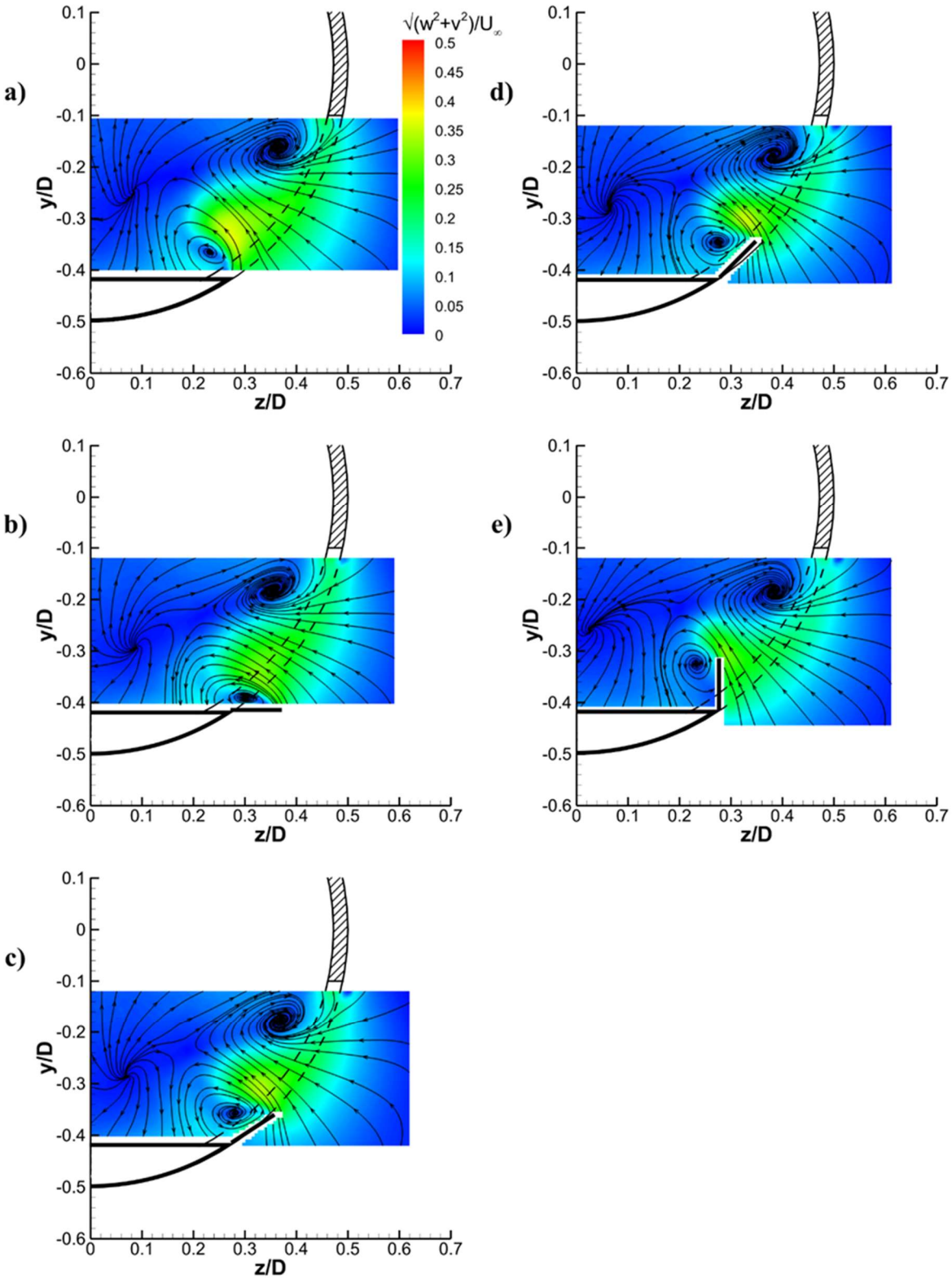

Figure 15: Time-averaged velocity with projected streamlines at x/L = 0.4 for a) l/L = 0.37 without flaps, b) θ = 0° flap, c) θ = 33° tangential flap, d) θ = 45° flap and e) θ = 90° vertical flap.

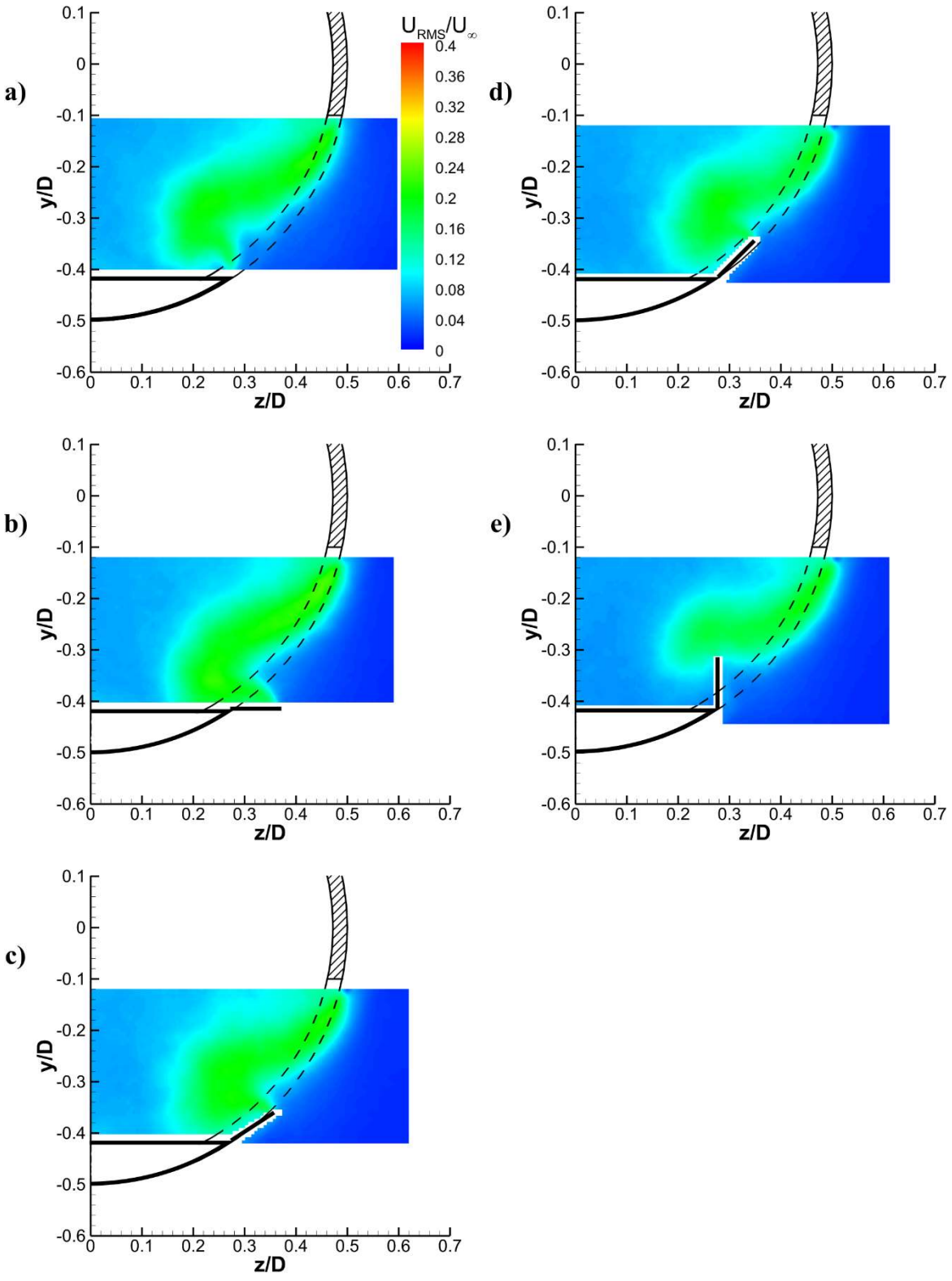

Figure 16: RMS of fluctuating velocity at $x/L = 0.4$ for. a) $l/L = 0.37$ without flaps, b) $\theta = 0°$ horizontal flap, c) $\theta = 33°$ tangential flap, d) $\theta = 45°$ flap and e) $\theta = 90°$ vertical flap.

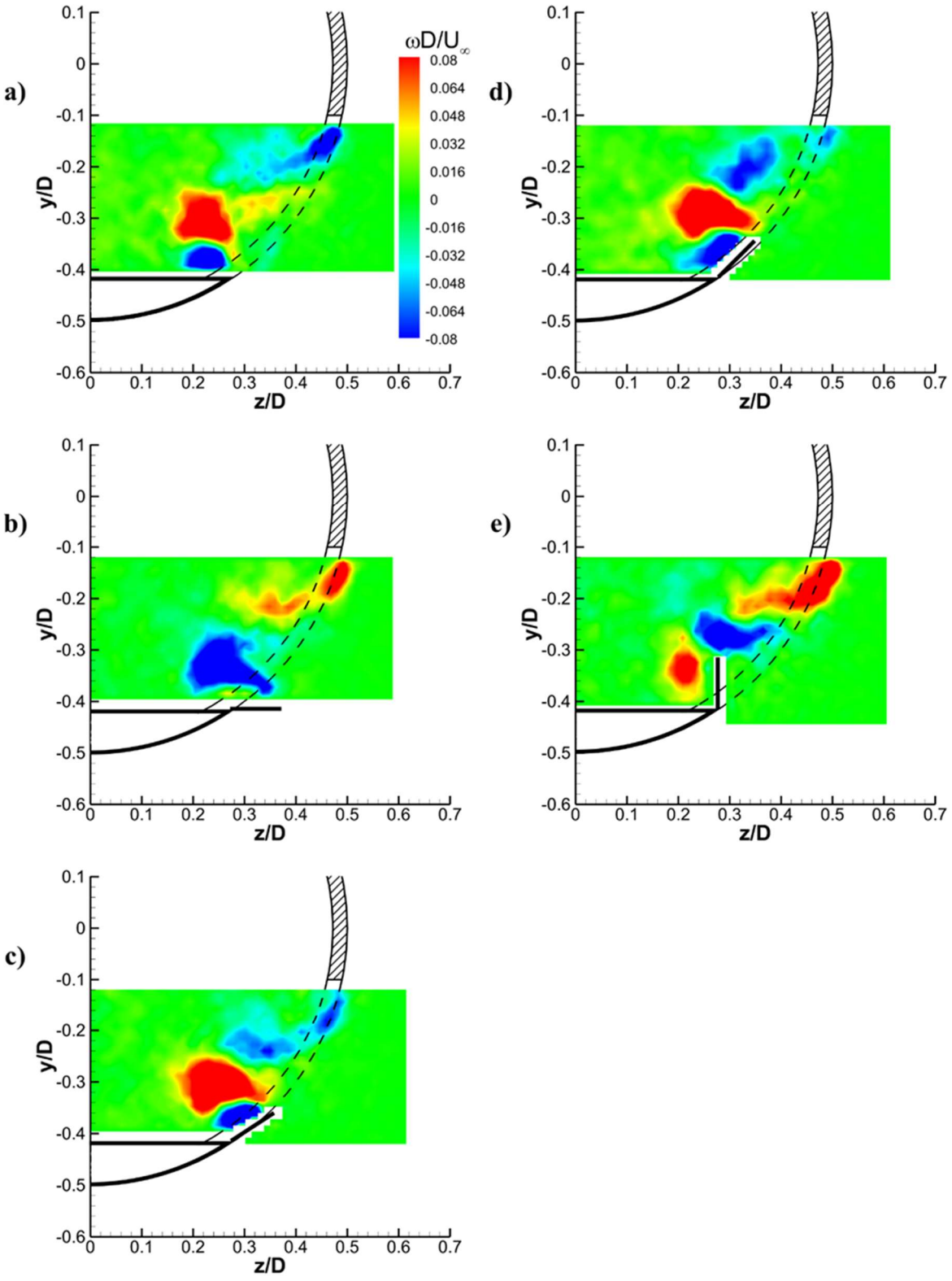

Figure 17: First POD mode at $x/L = 0.4$ for a) $l/L = 0.37$ without flaps, b) $\theta = 0°$ horizontal flap, c) $\theta = 33°$ tangential flap, d) $\theta = 45°$ flap and e) $\theta = 90°$ vertical flap.